# Nickel Particles Selectively Confined in the Mesoporous Channels of SBA-15 Yielding a Very Stable Catalyst for DRM reaction



| | |
|---|---|
| Journal: | *The Journal of Physical Chemistry* |
| Manuscript ID | jp-2017-03835h.R2 |
| Manuscript Type: | Special Issue Article |
| Date Submitted by the Author: | n/a |
| Complete List of Authors: | Rodriguez-Gomez, Alberto; Universidad de Sevilla Departamento de Quimica Inorganica<br>Pereñiguez, Rosa; CSIC,<br>Caballero, Alfonso; University of seville, Inorganic Chemistry |
| | |

# Nickel Particles Selectively Confined in the Mesoporous Channels of SBA-15 Yielding a Very Stable Catalyst for DRM Reaction

Alberto Rodriguez-Gomez, Rosa Pereñiguez and Alfonso Caballero*
*Instituto de Ciencia de Materiales de Sevilla (CSIC-University of Seville) and Departamento de Quimica Inorganica, University of Seville. Avda. Américo Vespucio, 49. 41092. Seville, Spain. caballero@us.es*

**Abstract**

A series of four Ni catalysts supported on SBA-15 and on a high $SiO_2$ surface area have been prepared by modified impregnation (ImU) and deposition-precipitation (DP) methods. The catalysts have been extensively characterized, including *in situ* XAS (bulk sensitive) and XPS (surface sensitive) techniques, and their catalytic activities evaluated in the dry reforming reaction of methane (DRM). The combined use of XPS and XAS has allowed to determine the location of nickel particles on each catalyst after reduction at high temperature (750 $^{o}$C). Both Ni/$SiO_2$-DP and Ni/SBA-15-DP catalysts yield well-dispersed and homogeneous metallic phases mainly located in the mesoporosity of both supports. By the contrary, the Ni/$SiO_2$-ImU and Ni/SBA-15-ImU catalysts present a bimodal distribution of the reduced nickel phase, with nickel metallic particles located out and into the mesoporous structure of $SiO_2$ or the SBA-15 channels.

The Ni/SBA-15-DP catalyst was found the most stable and performing system, with a very low level of carbon deposition, about an order of magnitude lower than the equivalent ImU catalyst. This outstanding performance comes from the confinement of small and homogeneous nickel particles in the mesoporous channels of SBA-15, which, in strong interaction with the support, are resistant to sintering and coke deposition during the demanding reaction conditions of DRM.

## 1. Introduction

Heterogeneous supported nickel catalysts have received a considerable attention in the last decades.[1-4] Although well known as the main catalytic system for the industrial steam reforming of hydrocarbons,[5-7] they are also important in other many catalytic reactions, both in well-established industrial processes as others being currently developed. Among the latter, the dry reforming of methane (DRM) using $CO_2$ as reactive has been extensively studied in the last years, especially after the recent and fast development of new gas natural extraction methodologies, such as the fracking processes.[8,9] As this greenhouse gas is often contained in natural gas fields, the DRM process consumes $CO_2$ while avoiding its emission to the atmosphere.[10-12] It is well known that this methane reaction proceeds on catalytic sites of the nickel metallic particles.[13] However, there are many known factors affecting the catalytic performance, mainly particle size and interaction with support surface.[13-19] Also, deposition of carbon over the catalyst, one of the main causes of deactivation, is extremely depending on the nickel particle properties and the interaction with the support.[20-25]

In this sense, the use of mesoporous supports has been proposed as good alternative for the improvement of catalytic performance.[26,27] Typically presenting a very high surface area and a variable size of the porosity,[28] these kind of materials could also play a role controlling the size of the metallic particles. Its location on the external surface of these supports or in their internal mesoporosity affects the shape and size of the metal particles, thus modifying the catalytic performance.[29]

The mesostructured silica SBA-15 has a high internal area, consisting on hexagonal pores with a mean diameter from 5 nm and framework walls of about 3-6 nm, presenting a remarkable hydrothermal and mechanical stability.[28] Considering the harsh reaction conditions needed for the DRM process, these characteristics make the SBA-15 suitable for the process, which at the same time can be used to obtain metallic particles within this size range, known appropriate to obtain high performance nickel catalysts.[30]

In this contribution, we have studied four nickel catalysts supported on two different mesoporous solids: a high surface area $SiO_2$, presenting a high amount of open mesoporous surface, and a SBA-15 silica support with the mesoporous channels

described below. In both cases, we have used two different preparation methodologies: an impregnation procedure (Ni/$SiO_2$-ImU and Ni/SBA-15-ImU samples) and a deposition-precipitation method (Ni/$SiO_2$-DP and Ni/SBA-15-DP samples). While the former is a well known method used for decades, the deposition-deposition precipitation one, although also currently well known, is relatively new and has been extensively used for preparing catalysts for DRM reaction.[31-33] In this way, we have succeeded to get systems with nickel particles located on the outer surface of the support nanoparticles, but also dispersed within the mesoporous surface of both supports. By using simultaneously two *in situ* spectroscopy techniques, one of them bulk sensitive (XAS) and the other one surface sensitive (XPS), we have been able to discriminate nickel phases in different locations; a NiO phase supported in the external surface, easily reducible and with a low interaction with the supports, and a second oxidized nickel phase located in the internal mesoporous structure which always interacts more strongly with the support, as reflected on their higher reduction temperature. These features have allowed us to correlate each nickel phase with the different behaviours under reaction conditions. The best catalytic performance has been obtained when the nickel particles are located in the mesoporous of the SBA-15 support.

## 2. Experimental

*Catalysts preparation*

A high surface area $SiO_2$ powder (Sigma-Aldrich, CAS: 112926-00-8) and a synthesized SBA-15 were used as supports. The mesoporous silica SBA-15 was prepared according to a method previously described in the literature,[34,35] using a molar relation of 1:0.02:9.91:320 TEOS:P123:HCl:$H_2O$ (TEOS: Sigma-Aldrich, CAS: 78-10-4; HCl: Sigma-Aldrich, CAS: 7647-01-0; Pluronic® P-123: Sigma-Aldrich, CAS: 9003-11-6). In a typical procedure, 18 g of P123 were dissolved in 270 mL of distilled water and under stirring, 135 mL of HCl in 540 mL of water were added. This solution was transferred into six glass bottles and heated up to 50 $^oC$. Under static conditions, 5.9 mL of TEOS were added in each bottle and kept at 50 $^oC$ for 18 h. After that, the white product obtained was filtered and washed with 6 L. of boiling distilled water. The

product was dried under vacuum at 70 $^{o}$C and calcined on static air for 3 hours at 550 $^{o}$C using a ramp of 1 $^{o}$C/min.

Active metal phase was introduced on both supports by two different methods. One of them consists of a deposition-precipitation method (DP) using urea (Alfa Aesar, CAS: 57-13-6) as a precipitant agent following a modified Liu et al. protocol.[36] Briefly, 1 g of calcined SBA-15 or $SiO_2$ was dispersed in 150 mL of $HNO_3$ 0.01M (Sigma-Aldrich, CAS: 7697-37-2) with the metal precursor $Ni(NO_3)_2{\cdot}6H_2O$ (Panreac, CAS: 13478-00-7). After 1 h stirring, 11.37 g of urea was added to the solution and the T increased up to 105 $^{o}$C under refluxing conditions. The mix was kept on stirring for 2 h before cooling it down to room temperature (RT). The dispersed powder was filtered and washed with distilled water and dried at 110 $^{o}$C for 24 h, and finally calcined on static air for 3 h at 550 $^{o}$C (using a ramp of 1 $^{o}$C/min). The resulting products were labelled as 10% Ni/SBA-15-DP and 10% Ni/$SiO_2$-DP respectively. A similar treatment without nickel was used to obtain the SBA-15-DP and $SiO_2$-DP modified supports. The 10% Ni/SBA-15-ImU and 10% Ni/$SiO_2$-ImU catalysts were prepared by incipient wetness impregnation assisted with ultrasound. Typically, 1 g of support was added to 1.8 mL of solution and mixed under ultrasound for 5 min., heated at 40 $^{o}$C overnight and finally calcined in 50 mL/min of argon at 550 $^{o}$C for 3 h using a heating ramp of 1 $^{o}$C /min.

*$N_2$-physisorption*

$N_2$ adsorption/desorption isotherms and BET surface areas were obtained at 77K using a TRISTAR II (Micromeritics) equipment. Catalytic systems were pre-treated under vacuum at 150 $^{o}$C prior to the adsorption/desorption experiment. Surface areas were calculated according to the BET method. Porosity was calculated by the BJH method.

*X-ray diffraction (XRD)*

Diffractograms for calcined and previously reduced samples were recorded in a PANalytical X-Pert PRO diffractometer with a Cu source ( λ=1.5418 Å, Cu Kα), working in a Bragg-Brentano configuration and equipped with an X'Celerator Detector, a real time multiple strip (RTMS) x-ray detector provided with an integrated array of parallel detectors allowing an up to 128-fold decrease in measurement time. (active range of 2

= 2.18°). The data acquisition was carried out in a 2θ range of 10-80°, a step of 0.05° and an acquisition time of 240 s, with a total adquisition time of 43 minutes.

*Temperature Programmed Reduction (TPR)*

The temperature-programmed reduction profiles were obtained using a thermal conductivity detector based in a Wheatstone bridge previously calibrated using commercial CuO. A 5%$H_2$/Ar calibrated mix was used as both carrier and reference gas (flow rate of 50 mL/min). An amount of sample that would consume approximately 100 µmol of $H_2$ was used for the experiment. Typically, the experiment was carried out from RT up to 900 $^{o}$C using a heating ramp of 10 $^{o}$C/min. All the experimental conditions were chosen to ensure that no peak coalescence occurred.[37]

*Transmission Electronic Microscopy (TEM)*

TEM images were obtained in a Philips CM200 microscope operating at 200 kV. Samples were dispersed on ethanol and deposited onto a copper grid coated with a lacey carbon film. Histograms for particle size distribution were obtained by sampling 150 particles.

*X-ray absorption spectroscopy (XAS)*

XAS (EXAFS and XANES regions) were recorded at the BL22 beamline (CLAESS) of ALBA synchrotron and the BM25A beamline (SPLINE) of ESRF synchrotron facilities. An optimum weight of sample to maximize the signal/noise ratio in the ionization chambers were pelletized through a hydraulic press of 13 mm at 3 tons and analysed in transmission mode in a multipurpose “in situ” cell for gas-solid reactions. XAS spectra were collected at different temperatures during treatments of the samples in 5%$H_2$/Ar flow (50 mL/min). A standard Ni-foil was measured and used for energy calibration. XAS spectra of Ni K-edge were recorded from 8200 to 9200 eV, with a step of 0.5 eV step across the XANES region. Once extracted from the XAS spectra, the EXAFS oscillations were Fourier transformed (F.T.) in the range 2.4–11.0 Å$^{-1}$. Spectra were analysed using the software package IFEFFIT.[38,39] The coordination number, interatomic distance, Debye–Waller factor and inner potential correction were used as variable parameters for the fitting procedures.

*X-ray photoelectron spectroscopy (XPS)*

XPS experiments were carried out in a VG-ESCALAB 210 equipment over pelletized samples. Samples were introduced in a pre-chamber at $10^{-7}$ Torr. Acquisition was performed in an appendant analysis chamber equipped with a SPECS Phoibos 100 hemispheric analyser at $10^{-9}$ Torr using Mg Kα radiation (E=1.5418 keV) with 20 mA of anode current and 12 kV of potential acceleration. Before acquisition, each sample was treated *in situ* at different T (350, 500 and 750 $^{o}$C) in a flow of 5%$H_2$/Ar at atmospheric pressure using a cell chamber attached to the above mentioned pre-chamber.

*Catalytic activity tests*

Dry reforming of methane (DRM) tests were performed using 20 mg of catalyst held in a tubular quartz reactor through wool quartz. The catalyst was mixed with 80 mg of SiC in order to avoid heat transport limitations. The catalytic systems were pre-treated in 5%$H_2$/Ar at 750 $^{o}$C for 1 h with a heating ramp of 10 $^{o}$C/min. Reaction was carried out with a not diluted mix (1:1) of 40 mL/min of $CH_4$ and 40 mL/min of $CO_2$ at 750 $^{o}$C during 42 h. Reaction products were analysed by GC using an Agilent´s 490 microGC equipped with three micro-columns, two molecular sieves, one of them using argon as carrier gas to detect $H_2$, and the second to detect methane and carbon monoxide with helium as carrier gas. The third was a polar column to analyse carbon dioxide and water. Each column was equipped with a TCD detector. The conversion and selectivities were calculated using the following equations:

$$CH_4\_conv(\%) = \frac{1-\frac{[CH_4]_{OUT}}{[CH_4]_{IN}}}{1+\frac{[CH_4]_{OUT}}{[CH_4]_{IN}}}100 \qquad CO_2\_conv(\%) = \frac{1-\frac{[CO_2]_{OUT}}{[CO_2]_{IN}}}{1+\frac{[CO_2]_{OUT}}{[CO_2]_{IN}}}100$$

$$H_2\_selectivity(\%) = \frac{[H_2]_{OUT}\left(1+\frac{CH_4\_conv(\%)}{100}\right)}{2\left([CH_4]_{IN}-[CH_4]_{OUT}\left(1+\frac{CH_4\_conv(\%)}{100}\right)\right)}100$$

*Thermogravimetric Analysis (TG)*

Thermal behaviour of the used catalysts was characterized in a thermogravimetric analyser (TA SDT Q600). Experiments were carried out within a T range of 25-900 $^{o}$C in air under a dynamic atmosphere (flow rate of 100 mL/min) and a heating rate of 10 $^{o}$C/min. The mass of catalyst was 5 mg. Results of the measurements were evaluated online using the SDT Q600 software.

## 3. Results and discussion

*3.1. Physical and chemical characterization of calcined systems*

After the calcination treatment of the freshly prepared samples, they were submitted to a characterization study by $N_2$ adsorption analysis (BET, BJH), XRD, TEM, XAS and XPS. The adsorption isotherms obtained for all the systems were type-IV, typical for mesoporous materials. However, as reflected in Table 1 significant differences in BET surface area and mean porous size are observed. In the case of SBA-15 support, the impregnated sample reduces the specific surface about a 40% (from 698 to 440 $m^2$/g), while the urea treatment accomplished during the DP process of nickel (also done without nickel as a blank) gives rise to an important surface decrease of around 60%, with the simultaneous collapse of the smaller porosity (mean size increasing from 6.7 to 9.0 nm). Values are lower for the $SiO_2$ support: a surface reduction of 15% after impregnation (from 534 to 451 $m^2$/g), and of 40% after urea treatments (with or without nickel). Finally, the porosity partially collapses after the urea treatment (mean size increasing from 4.3 to 8.0 nm).

The images obtained by TEM, as those included in Figure 1, show important differences between the four calcined systems. Both DP samples (labels a-b) seem to present the characteristic “fibrous” microstructures of nickel phyllosilicate phase,[40,41] overlapped with the porous structure of the SBA-15 and the $SiO_2$, respectively. The

XRD diagrams in Figure 2 confirm the presence of a nickel phyllosilicate phase, identified by the peaks at 34, 37 and 61°. No peaks from a NiO phase could be detected. The TEM images of the two ImU catalysts (Figure 1, labels c-d) show black spots which are clearly identified as a NiO phase by XRD (Figure 2, peaks at 37, 43 and 63°). The assignment of these phases for both Ni/SBA-15 catalysts has been confirmed by XAS spectroscopy. As shown in Figure 3, the XANES spectrum of the ImU sample, and specially the white line, is characteristic of NiO[42] and different from that of Ni/SBA-15-DP sample, which correspond to the nickel silicate identified below. Also, the Fourier Transforms (Figure 3, right) obtained from the EXAFS of calcined Ni/SBA-15-ImU sample clearly corresponds to NiO, with a very intense peak centered at 2.83 Å from Ni-Ni second neighbour of the cubic phase.[42] At 2.93 Å appears the equivalent Ni-Si contribution for the phyllosilicate in the Ni/SBA-15-DP catalyst.[43,44]

Finally, the XPS data have shed additional light on the physical and chemical state of these calcined catalysts. As pointed out in Figure 4, XPS show different position for the main peak of calcined DP and ImU samples, 856.6 eV and 855.1 eV respectively, which can again be ascribed to the presence of, respectively, nickel phyllosilicate and NiO phases.[44,45] It is also interesting to remark on the intensity differences (Table 1) depending on the support ($SiO_2$ or SBA-15) and on the preparation method (ImU or DP). These intensities are about an order of magnitude higher for both Ni supported DP systems, which must be related to a better dispersion of the nickel oxidized phase over the supports, as reflected in Table 1. It is also interesting to note that Ni/$SiO_2$-ImU signal is more intense than the equivalent Ni/SBA-15-ImU catalyst, once again in agreement with the crystallite sizes of the nickel oxide particles in the calcined samples determined by XRD (Table 1).

*3.2. Study of the reduction processes and the reduced catalytic systems*

The reduction of the oxidized nickel phases has been monitored by TPR. As shown in Figure 5, the profiles of ImU and DP catalysts present very different features. Both DP samples have similar profiles, with a main peak at around 660 °C, previously assigned to a nickel phyllosilicate phase,[43] and an additional wide, small shoulder centered at about 400 °C, a temperature range characteristic of NiO reduction. Similarly, just as previously reported,[26] the ImU samples present also two peaks, in

these cases at lower temperature and with similar intensities. In Ni/SBA-15-ImU these peaks are centered at 375 and 525 $^{o}$C, and in Ni/$SiO_2$-ImU centered at 375 and 460 $^{o}$C. As the XRD diagram of these samples (Figure 2) showed that only NiO is present in both ImU catalysts, these two peaks must correspond to two different NiO phases coexisting within the catalysts with different degrees of interaction with the supports. The first one, reducing at lower temperature, seems to be similar to massive NiO. The second one, with a higher reduction temperature, must correspond to a NiO phase interacting more strongly with the supports.[46] The observed differences in the TPR profiles of both ImU samples can be related with the slightly different particle size ranges (Table 1), but also considering that particles with similar size present a stronger interaction when located inside the mesoporous channel of SBA-15 support. The results of these reduction processes are reflected both in the XRD diagrams of Figure 2 and the TEM images of Figure 6. Both DP samples generate small and homogeneous nickel particles of about 4-6 nm (Table 1, calculated from Scherrer formula and Figure 7 evaluated from TEM images). It is worth to note that in Ni/SBA-15-DP, many nickel particles seem to be aligned with the mesoporous channels of support, but also encapsulated in a phase of amorphous appearance, which must come from the partial solution of SBA-15 during the deposition-precipitation process.[45,47] The state of impregnated Ni/SBA-15-ImU and Ni/$SiO_2$-ImU samples are completely different, with a mean diameter particles around 15-20 nm (Table 1, Scherrer calculation), but heterogeneously distributed. The analysis of TEM images (Figure 7) shows a large number of particles with a diameter between 5-15 nm, and a relatively small number of larger particles of 25-35 nm, and even larger than that for the silica supported system.

The reduction processes of both SBA-15 supported catalysts have been also analysed by *in situ* XAS spectroscopy. Figure 8 shows the XANES and F.T. of the EXAFS spectra obtained for the Ni/SBA-15-ImU catalyst at RT (after calcination), during hydrogen reduction at 500 $^{0}$C and at RT after the hydrogen reduction treatment at 750 $^{o}$C. As indicated before, the XANES of the calcined sample, characteristic of a NiO phase evolves after reduction at 500 $^{o}$C to an almost completely reduced metallic nickel phase. Only the slightly more intense white line reveals the presence of a small proportion of remaining nickel oxide. The reduction treatment at 750 $^{o}$C yields a

completely reduced nickel phase.[17] Using the XANES spectra of an oxidized and metallic references, a linear combination procedure of the XANES spectra obtained after treatment with hydrogen at 500 $^{o}$C has allowed us to estimate a reduction percentage of 90% for this ImU sample (Table 2). As shown in Figure 9, where these reduction temperatures are tagged in the TPR profiles, overall these results are as expected. The F.T. obtained from the EXAFS region (Figure 8, right) also show consistent results. The two main peaks at 1.8 and 2.83 Å obtained for the calcined Ni/SBA-15-ImU sample are characteristic of a NiO phase.[2] Also, the spectrum obtained at 500 $^{o}$C, with a main peak at 2.50 Å, agrees with the TPR profile, indicating virtually total nickel reduction. In this sense, it is important to note that the differences in intensities observed for both reducing treatments come from the different temperatures of the spectra acquisition: 500 $^{o}$C and room temperature, respectively, which change the amplitude of the EXAFS oscillation through the Debye-Waller factors. By EXAFS spectrum fitting analysis of the totally reduced Ni/SBA-15-ImU catalyst, a value of 11.6 has been obtained for the Ni-Ni coordination number (CN), close to the value 12 of bulk nickel, which is also compatible with particles larger than 10 nm in diameter, as previously obtained by Scherrer and TEM images (Table 1).

The behaviour of the Ni/SBA-15-DP catalyst is drastically different. As shown in Figure 10, the original XANES of the DP sample characteristics of nickel silicate undergoes only small changes after reduction at 500 $^{o}$C, with only a small fraction of reduced nickel (25%, obtained by linear combination, Table 2). Finally, in agreement with TPR (Figure 9) at 750 $^{o}$C nickel appears completely reduced. The mean Ni-Ni coordination number of 10.6 obtained by fitting analysis of the EXAFS spectrum also agrees with TEM and XRD data (Table 1), indicating the presence of smaller nickel particles.

Although a similar XAS study over both Ni/$SiO_2$ samples has not been done because of beam time availability, considering the previous TPR and XRD results exhibit above, a similar behaviour to the Ni/SBA-15 catalysts could be expected for these two catalysts.

As previously shown for DP samples,[48] the characterization of reduction processes by *in situ* XPS gives seemingly contradictory results. Figure 11 includes the

XPS obtained for the different catalysts under the indicated *in situ* conditions: samples calcined and after hydrogen reduction at 350, 500 and 750 $^{o}$C, respectively. As discussed above (Figure 4), spectra of both calcined ImU samples are characteristic of NiO, while the corresponding two DP samples show spectra attributed to $Ni^{2+}$ species of a phyllosilicate phase.[44,45]

With respect to the two ImU samples, it is noteworthy the different behaviour of both catalysts after the hydrogen treatments. While the Ni/SBA-15-ImU sample appears completely reduced at 350 $^{o}$C, without further major changes at temperatures up to 750 $^{o}$C, the Ni/$SiO_2$-ImU catalysts is only partially reduced at the lowest temperature, being completely reduced at 500 $^{o}$C. According to the TPR profiles in Figure 9, at this low temperature of 350 $^{o}$C most of nickel should remain oxidized in both ImU catalysts, especially in the SBA-15 supported sample whose TPR profile extends at even higher temperature. However, considering the surface sensitivity of the XPS technique, this result indicates that the small fraction of nickel reduced at 350 $^{o}$C in the Ni/SBA-15-ImU sample must correspond to NiO on the surface support. Accordingly, the unreduced fraction, undetectable by XPS, must be located at the inner surface of the mesoporous channels. A similar interpretation can be done for the Ni/$SiO_2$-ImU samples, but in this case the NiO particles reducing above 350 $^{o}$C must be located in the mesoporous of the $SiO_2$ support, which as external porosity, are partially visible by XPS.

In the same way, the behaviour of both DP samples after the hydrogen treatments does not seem to agree with the previous TPR and XAS results. At 350 $^{o}$C, the reduction process has not begun (Figure 9), and according to the XPS spectra of Figure 11, the nickel remains completely oxidized in both catalysts. However, at 500 $^{o}$C virtually all the nickel appears reduced to the metallic state in both DP catalysts, but according to the TPR profiles, only the small fraction of nickel reduced at the small shoulder centered at 350 $^{o}$C should be affected by this reduction treatment. Considering the surface sensitive of XPS, these results are indicating that the nickel species reducing at the lowest temperature range must be located in the outer surface of the supports. So, once again, the main peak centered at 660 $^{o}$C corresponds in these cases to the reduction of nickel species confined into the mesoporous surface, channels and open mesoporosity, respectively.

In summary, these results so far presented allowed us to assign each TPR contribution to different kind of oxidized nickel phases located in different positions in the four catalysts prepared with the SBA-15 and $SiO_2$ mesoporous supports.

*3.3. Catalytic studies*

The four catalytic systems were tested in the dry reforming reaction of methane (DRM). As shown in Figure 12, the catalytic performances differ drastically depending on the support and the preparation method. It is worth pointing out the excellent performance, both in activity and stability, of Ni/SBA-15-DP after 40 hours under this harsh reaction conditions (undiluted mixture of methane and $CO_2$). It can be observed that also the $H_2$/CO ratio around 0.9 is constant during the whole period. The two ImU samples supported on SBA-15 and $SiO_2$ showed a similar behaviour, with a relatively high initial activity (35-45% methane conversion) and a high deactivation rate, reaching -after 40 hours- methane conversion values of 20-25%. At the same time, the $H_2$/CO ratios are extremely low, especially in the Ni/$SiO_2$-ImU sample with a value of $H_2$/CO of 0.3 after 40 h of TOS. This indicates an important contribution of the reverse WGSR ($CO_2 + H_2 \rightleftharpoons CO + H_2O$), which increases the production of CO, decreasing the amount of hydrogen as product. Finally, the Ni/$SiO_2$-DP presented a mixed behaviour, with initial values similar to Ni/SBA-15-DP but quickly declining to conversion values close to those of the ImU catalysts. Interestingly, also the $H_2$/CO ratio, related with the RWGS reaction evolves during reaction in this catalyst. Considering that as will be show below, the nickel particle size of this catalyst increases during reaction, these findings seem to indicate that in our catalyst large particle sizes favours this RWGS reaction.

After 40 hours under reaction conditions, the catalyst presented the appearance showed in the TEM images of Figure 13. Nickel particles have clearly increased their sizes in all catalysts with the exception of the Ni/SBA-15-DP catalyst. This size stability, which should be related to the nickel particles confinement in the mesoporous channels of the SBA-15 support, must account for the noticeable stability in the catalytic performance. It is also worth mentioning that the bimodal catalytic behaviour of Ni/$SiO_2$-DP can be explained considering that this catalyst contains

initially small nickel particles similar to those detected in the Ni/SBA-15-DP. During reaction, the size of these particles increases, now presenting a lower catalytic performance. It is also relevant to remark that no carbon deposits could be observed in the image of Ni/$SiO_2$-ImU, which will be confirmed by the TG/DSC included below.

Thus, Figure 14 include the results from Thermogravimetric Analysis (TG) and Differential Scanning Calorimetry (DSC). As shown, while the Ni/SBA-15-ImU catalyst contains a higher amount of carbon than the DP which according to the TG/DSC, must correspond to a graphitic coke more difficult to oxidize.[49-52] The Ni/SBA-15-DP presents a less amount of coke and a lower combustion temperature. On the other hand, the analogous Ni/$SiO_2$ samples present much less carbon, especially the impregnated one, which does not present carbon deposits at all. This surprising behaviour could be explained considering two different facts. First of all, this sample has a low methane conversion level, which implies that less amount of methane has been transformed. The second factor could be the high activity of this sample in the RWGS reaction. As shown in figure 12, the value of $H_2$/CO=0.3 impies that an amount of water is also generated, which could contributed to the elimination of carbon through the steam reforming reaction of this carbon deposits. Also, it is especially relevant the quantification of carbon deposits in relation with the total volume of methane converted during the 40 hours period. This amount (Figure 14) is an order of magnitude smaller in both DP catalysts which together with the less harmful nature of its coke in the SBA-15 supported one, can explain the extremely stable catalytic behaviour of this catalyst, standing out from the other studied catalysts.

**4. Conclusions**

In this work, we have characterized a number of nickel catalysts using two different preparation methods and two different mesoporous supports, namely a SBA-15 and a high surface mesoporous $SiO_2$.

All results together, it has been concluded that the formation of a nickel silicate phase confined in the inner surface of mesoporous SBA-15 support gives rise after reduction to well dispersed metallic nickel particles in strong interaction with the support. This inner nickel phase has been unambiguously identified by the

combination of a number of techniques, especially *in situ* XPS and XAS, able to detect respectively, species exclusively located at the surface and at the bulk of the supports. The interaction generated in this Ni/SBA-15-DP system between the nickel particles and the mesoporous channels of the SBA-15 support ensures a stable catalytic performance under the harsh reaction conditions of DRM, with no evident signs of sintering and a lower amount of coke deposits than the analogous ImU catalyst.. These conclusions are also reinforced considering the parallel evolution of catalytic performance and nickel particle size of the $Ni/SiO_2$-DP catalyst during reaction: these are similar to the analogous SBA-15 catalyst during the initial stage of reaction, reaching after 40 hours under DRM reaction a size and catalytic behavior closer to that of both ImU catalysts.

*Acknowledgments*

We thank the FEDER program and the "Ministerio de Economia y Competitividad" of Spain (Projects ENE2011-24412 and CTQ2014-60524-R) for funding this research. Also, we thank the ESRF facility and staff (BM25 SPLINE beamline) and ALBA facility and staff (BL22 CLAESS beamline) for their experimental support. A.R.G thanks also the Spanish Government for the PhD fellowship (BES-2012-061744).

*References*

1. Ananikov, V. P. Nickel: The "Spirited Horse" of Transition Metal Catalysis. *ACS Catalysis*, **2015**, *5*, 1964–1971.

2. Gonzalez-Delacruz, V. M.; Pereñiguez, R.; Ternero, F.; Holgado, J. P.; Caballero, A. Modifying the Size of Nickel Metallic Particles by $H_2$/CO Treatment in $Ni/ZrO_2$ Methane Dry Reforming Catalysts. *ACS Catalysis*, **2011**, *1*, 82–88.

3. Pakhare, D.; Spivey, J. A review of dry ($CO_2$) reforming of methane over noble metal catalysts. *Chemical Society Reviews*, **2014**, *43*, 7813-7837.

4. Rostrup-Nielsen, J. R. Fuels and Energy for the Future: The Role of Catalysis. *Catalysis Reviews*, **2004**, *46*, 247-270.

5. Oyama, S. T.; Hacarlioglu, P.; Gu, Y. F.; Lee, D. Dry reforming of methane has no future for hydrogen production: Comparison with steam reforming at high pressure in

standard and membrane reactors. *International Journal of Hydrogen Energy*, **2012**, *37*, 10444-10450.

6. Bhavani, A. G.; Kim, W. Y.; Lee, J. S. Barium Substituted Lanthanum Manganite Perovskite for $CO_2$ Reforming of Methane. *ACS Catalysis,* **2013**, *3*, 1537-1544.

7. Nguyen, T. H.; Łamacz, A.; Krztoń, A.; Liszka, B.; Djéga-Mariadassou, G. Partial oxidation of methane over $Ni^0/La_2O_3$ bifunctional catalyst III. Steady state activity of methane total oxidation, dry reforming, steam reforming and partial oxidation. Sequences of elementary steps. *Applied Catalysis B: Environmental,* **2016**, *182*, 385-391.

8. Albarazi, A.; Beaunier, P.; Da Costa, P. Hydrogen and syngas production by methane dry reforming on SBA-15 supported nickel catalysts: On the effect of promotion by $Ce_{0.75}Zr_{0.25}O_2$ mixed oxide. *International Journal of Hydrogen Energy,* **2013**, *38*, 127-139.

9. Wang, Q.; Chen, X.; Jha, A. N.; Rogers, H. Natural gas from shale formation – The evolution, evidences and challenges of shale gas revolution in United States. *Renewable and Sustainable Energy Reviews*, **2014**, *30*, 1–28.

10. Lin, H.; Van Wagner, E.; Raharjo, R.; Freeman, B. D.; Roman, I. High-performance polymer membranes for natural-gas sweetening. *Adv. Mater.,* **2006**, *18*, 39-44.

11. Bradford, M. C. J.; Vannice, M. A. $CO_2$ reforming of methane. *Catal. Rev*., **1999**, *41*, 1-42.

12. Kumar, N.; Shojaee, M.; Spivey, J. J. Catalytic bi-reforming of methane: From greenhouse gases to syngas. *Current Opinion in Chemical Engineering*, **2015**, *9*, 8–15.

13. Wei, J.; Iglesia, E. Isotopic and kinetic assessment of the mechanism of reactions of $CH_4$ with $CO_2$ or $H_2O$ to form synthesis gas and carbon on nickel catalysts. *Journal of Catalysis*, **2004**, *224*, 370-383.

14. Jose-Alonso, D. S.; Illan-Gomez, M. J.; Roman-Martinez, M. C. Low metal content Co and Ni alumina supported catalysts for the $CO_2$ reforming of methane. *International Journal of Hydrogen Energy*, **2013**, *38*, 2230-2239.

15. Xu, B. Q.; Wei, J. M.; Wang, H. Y.; Sun, K. Q.; Zhu, Q. M. Nano-MgO: novel preparation and application as support of Ni catalyst for $CO_2$ reforming of methane. *Catalysis Today*, **2001**, *68*, 217-225.

16. Liu, D. P.; Quek, X. Y.; Cheo, W. N. E.; Lau, R.; Borgna, A.; Yang, Y. H. MCM-41 supported nickel-based bimetallic catalysts with superior stability during carbon dioxide reforming of methane: Effect of strong metal–support interaction. *Journal of Catalysis*, **2009**, *266*, 380-390.

17. Gonzalez-Delacruz, V. M.; Holgado, J. P.; Pereñiguez, R.; Caballero, A. Morphology changes induced by strong metal–support interaction on a Ni–ceria catalytic system. *Journal of Catalysis*, **2008**, *257*, 307–314.

18. Pereñiguez, R.; Gonzalez-Delacruz, V. M.; Holgado, J. P.; Caballero, A. Synthesis and characterization of a $LaNiO_3$ perovskite as precursor for methane reforming reactions catalysts. *Applied Catalysis B: Environmental*, **2010**, *93*, 346–353.

19. Zhu, J. Q.; Peng, X. X.; Yao, L.; Shen, J.; Tong, D. M.; Hu, C. W. The promoting effect of La, Mg, Co and Zn on the activity and stability of $Ni/SiO_2$ catalyst for $CO_2$ reforming of methane. *International Journal of Hydrogen Energy*, **2011**, *36*, 7094-7104.

20. Chen, D.; Lodeng, R.; Anundskas, A.; Olsvik, O.; Holmen, A. Deactivation during carbon dioxide reforming of methane over Ni catalyst: microkinetic analysis. *Chem. Eng. Sci.*, **2001**, *56*, 1371-1379.

21. Oemar, U.; Kathiraser, Y.; Mo, L.; Ho X.; Kawi, S. $CO_2$ reforming of methane over highly active La-promoted Ni supported on SBA-15 catalysts: mechanism and kinetic modelling. *Catal. Sci. Technol.*, **2016**, *6*, 1173-1186.

22. Liu, J.; Peng, H.; Liu, W.; Xu, X.; Wang, X.; Li, C.; Zhou, W.; Yuan, P.; Chen, X.; Zhang, W. Tin Modification on $Ni/Al_2O_3$: Designing Potent Coke-Resistant Catalysts for the Dry Reforming of Methane. *ChemCatChem*, **2014**, *6*, 2095-2104.

23. Smolakova, L.; Kout, M.; Capek, L.; Rodriguez-Gomez, A.; Gonzalez-Delacruz, V. M.; Hromadko, L.; Caballero, A. Nickel catalyst with outstanding activity in the DRM reaction prepared by high temperature calcination treatment. *International Journal of Hydrogen Energy,* 2016, *41*, 8459-8469.

24. Theofanidis, S.A.; Galvita, V. V.; Poelman, H.; Marin, G. B. Enhanced Carbon-Resistant Dry Reforming Fe-Ni Catalyst: Role of Fe. *ACS Catalysis*, **2015**, 5, 3028-3039.

25. Elsayed, N. H.; Roberts, N. R.; Joseph, B.; Kuhn, J. N. Low temperature dry reforming of methane over Pt–Ni–Mg/ceria–zirconia catalysts. *Applied Catalysis B: Environmental*, **2015**, *179*, 213-219.

26. Tao, M.; Xin, Z.; Meng, X.; Lv, Y.; Bian, Z. Impact of double-solvent impregnation on the Ni dispersion of Ni/SBA-15 catalysts and catalytic performance for the syngas methanation reaction. *RSC Advances*, **2016**, *6*, 35875.

27. Gálvez, M.E.; Albarazi, A.; Da Costa, P. Enhanced catalytic stability through non-conventional synthesis of Ni/SBA-15 for methane dry reforming at low temperatures. *Applied Catalysis A: General*, **2015**, *504*, 143–150.

28. Thielemann, J. P.; Girgsdies, F.; Schlögl, R.; Hess, C. Pore structure and surface area of silica SBA-15: influence of washing and scale-up. *Beilstein Journal of Nanotechnology*, **2011**, *2*, 110–118.

29. Trong On, D.; Desplantier-Giscard, D.; Danumah, C.; Kaliaguine, S. Perspectives in catalytic applications of mesostructured materials. *Applied Catalysis A: General*, **2001**, *222*, 299–357.

30. Vizcaíno, A. J.; Carrero, A.; Calles, J. A. Comparison of ethanol steam reforming using Co and Ni catalysts supported on SBA-15 modified by Ca and Mg. *Fuel Processing Technology*, **2016**, *146*, 99–109.

31. Burattin, P.; Che, M.; Louis, C. Ni/$SiO_2$ Materials Prepared by Deposition-Precipitation: Influence of the Reduction Conditions and Mechanism of Formation of Metal Particles. *Journal of Physical Chemistry B*, **2000**, *104*, 10482-10489.

32. Zhang, Q.; Wang, M.; Zhang, T.; Wang, Y.; Tang, X.; Ning, P. A stable Ni/SBA-15 catalyst prepared by the ammonia evaporation method for dry reforming of methane. *RSC Advances*, **2015**, *5*, 94016-94024.

33. Majewski, A. J.; Wood, J.; Bujalski, W. Nickel–silica core@shell catalyst for methane reforming. *International Journal of Hydrogen Energy*, **2013**, *38*, 14531-14541.

34. Acatrinei, A. I., Hartl, M. A., Eckert, J., Falcao, E. H. L., Chertkov, G., Daemen, L. L. Hydrogen Adsorption in the Ti-Doped Mesoporous Silicate SBA-15. *Journal of Physical Chemistry C*, **2009**, *113*, 15634-15638.

35. Zhao, D. Y., Feng, J. L., Huo, Q. S., Melosh, N., Fredrickson, G. H., Chmelka, B. F., Stucky, G. D. Triblock Copolymer Syntheses of Mesoporous Silica with Periodic 50 to 300 Angstrom Pores. *Science*, **1998**, *279*, 548-552.

36. Liu, H. C., Wang, H., Shen, J. G., Sun, Y., Liu, Z. M. Preparation, characterization and activities of the nano-sized Ni/SBA-15 catalyst for producing COx-free hydrogen from ammonia. *Applied Catalysis A: General*, **2008**, *337*, 138-147.

37. Malet P., Caballero A. The Selection of Experimental Conditions in Temperature Programmed Reduction Experiments. *Chem. Soc. Faraday Trans.,* **1988**, 84, 2369-2375.

38. M. Newville, J. IFEFFIT: Interactive XAFS analysis and FEFF fitting. *Synchrotron Radiation*, **2001**, *8*, 322-324.

39. Ankudinov, A. L.; Rehr, J. J. Relativistic calculations of spin-dependent x-ray-absorption spectra. *Physical Review B,* **1997**, *56*, R1712-1715.

40. Zhang, C.; Yue, H.; Huang, Z.; Li, S.; Wu, G.; Ma, X.; Gong, J. Hydrogen Production via Steam Reforming of Ethanol on Phyllosilicate-Derived Ni/$SiO_2$: Enhanced Metal–Support Interaction and Catalytic Stability. *ACS Sustainable Chem. Eng.,* **2012**, *1*, 161−173.

41. Kong, X.; Zhu, Y.; Zheng, H.; Li, X.; Zhu, Y.; Li, Y. W. Ni Nanoparticles Inlaid Nickel Phyllosilicate as a Metal–Acid Bifunctional Catalyst for Low-Temperature Hydrogenolysis Reactions. *ACS Catalysis*, **2015**, *5*, 5914-5920.

42. Gonzalez-Delacruz, V. M.; Pereñiguez, R.; Ternero, F.; Holgado, J. P.; Caballero, A. In Situ XAS Study of Synergic Effects on Ni–Co/$ZrO_2$ Methane Reforming Catalysts. *Journal of Physical Chemistry C*, **2012**, *116*, 2919–2926.

43. Burattin, P.; Che, M.; Louis, C. Characterization of the Ni(II) Phase Formed on Silica Upon Deposition−Precipitation. *Journal of Physical Chemistry B*, **1997**, 101, 7060-7074.

44. Espinos, J. P.; Gonzalez-Elipe, A. R.; Caballero, A.; Garcia, J. Munuera, G. The state of nickel in Ni/$SiO_2$ and Ni/$TiO_2$-calcined catalysts. *Journal of Catalysis*, **1992**, *136*, 415-422.

45. Lu, B. ; Ju, Y. ; Abe, T.; Kawamoto, K. Grafting Ni particles onto SBA-15, and their enhanced performance for $CO_2$ methanation. *RSC Advances*, **2015**, *5*, 56444–56454.

46. Huang, F.; Wang, R.; Yang, C.; Driss, H.; Chu, W. Zhang, H. Catalytic performances of Ni/mesoporous SiO 2 catalysts for dry reforming of methane to hydrogen. *Journal of Energy Chemistry*, **2016**, *25*, 709-719.

47. Burattin, P.; Che, M.; Louis, C. Molecular Approach to the Mechanism of Deposition−Precipitation of the Ni(II) Phase on Silica. *Journal of Physical Chemistry B*, **1998**, *102*, 2722-2732.

48. Rodriguez-Gomez, A.; Caballero, A. Identification of Outer and Inner Nickel Particles in a Mesoporous Support: How the Channels Modify the Reducibility of Ni/SBA-15 Catalysts. *ChemNanoMat*, **2017**, *3*, 94-97.

49. Wang, C. Z.; Sun, N. N.; Zhao, N.; Wei, W.; Sun, Y. H.; Sun, C. G.; Liu, Y. H.; Snape, C. E. Coking and deactivation of a mesoporous Ni–CaO–$ZrO_2$ catalyst in dry reforming of methane: A study under different feeding compositions. *Fuel*, **2015**, *143*, 527-535.

50. Bao, Z.; Lu, Y.; Han, J.; Li, Y.; Yu, F. Highly active and stable Ni-based bimodal pore catalyst for dry reforming of methane. *Applied Catalysis A: General*, **2015**, *491*, 116-126.

51. Carrero, A.; Calles, J. A.; Vizcaino, A. J. Effect of Mg and Ca addition on coke deposition over Cu–Ni/$SiO_2$ catalysts for ethanol steam reforming. *Chemical Enginnering Journal*, **2010**, *163*, 395-402.

52. Vicente, J.; Ereña, J.; Montero, C.; Azkoiti, M. J.; Bilbao, J.; Gayubo, A. G. Reaction pathway for ethanol steam reforming on a Ni/$SiO_2$ catalyst including coke formation. *International Journal of Hydrogen Energy*, **2014**, *39*, 18820-18834.

**TOC Graphic**

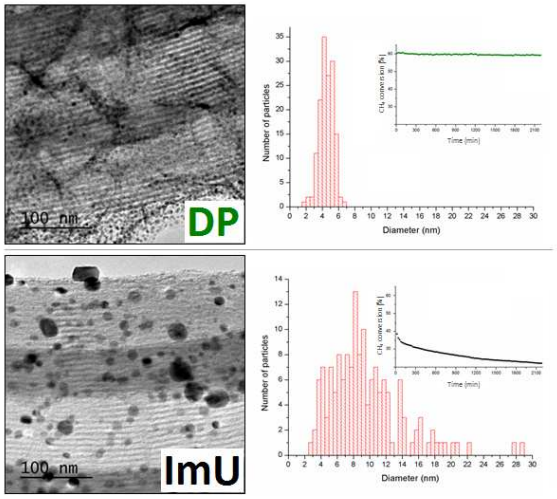
100 nm
DP
Number of particles
Diameter (nm)
Time (min)
100 nm
ImU
Number of particles
Diameter (nm)
Time (min)

**Table 1**
Specific surface areas and average pore size obtained from $N_2$-adsorption/desorption isotherms, nickel atomic percentage calculated from XPS spectra, average crystallite size by the Scherrer equation and average particle size by TEM, for the different supports and Ni-based systems.

| | $S_{BET}$ ($m^2 \cdot g^{-1}$) | Average pore size (nm)[a] | $Ni_{surf.}$ by XPS ($\%_{at}$) | Average NiO/Ni crystallite size (XRD[b]) | Average Ni particle size (TEM[c]) |
|---|---|---|---|---|---|
| SBA-15 | 698 | 6.7 | - | - | - |
| Ni/SBA-15 ImU [calcined/$H_2$,750°C] | 440/338 | 6.5/7.2 | 0.68/0.38 | 17.0/16.7 | - /9.7 |
| SBA-15 treated with urea | 749 | 9.1 | - | - | - |
| Ni/SBA 15 DP [calcined/$H_2$,750°C] | 301/265 | 8.8/10.7 | 11.27/1.81 | 5.7/3.7 | /4.4 |
| Commercial $SiO_2$ | 534 | 4.3 | - | - | - |
| Ni/$SiO_2$ ImU [calcined/$H_2$,750°C] | 451/433 | 4.5/4.3 | 0.86/0.42 | 11.0/19.5 | - /21.7 |
| Commercial $SiO_2$ treated with urea | 331 | 8.2 | - | - | - |
| Ni/$SiO_2$ DP [calcined/$H_2$,750°C] | 331/240 | 6.3/7.1 | 5.05/1.38 | 6.1/3.6 | - /5.7 |

[a] Obtained by the BJH method.
[b] Calculed from the Scherrer equation.
[c] Obtained by sampling 150 particles.

**Table 2.**
Percentage of $Ni^0$ calculated by linear combination of XANES spectra and best fitting values obtained from the EXAFS of reduced samples

| | $Ni^0$ at 500°C in $H_2$ (%)[a] | $Ni^0$ at 750°C in $H_2$ (%)[a] | C.N.[b] | $\Delta E^o$ (eV) | $R^b$ (Å) | D-W ($Å^2x10^{-3}$) |
|---|---|---|---|---|---|---|
| Ni/SBA-15 ImU | 90 | 100 | 11.4 | 6.8 | 2.47 | 6 |
| Ni/SBA-15 DP | 25 | 100 | 10.2 | 6.7 | 2.47 | 6 |

[a] Calculed by linear combination of XANES spectra
[b] Referred to C.N. of 12 and R of 2.48Å of a reference Ni-Foil

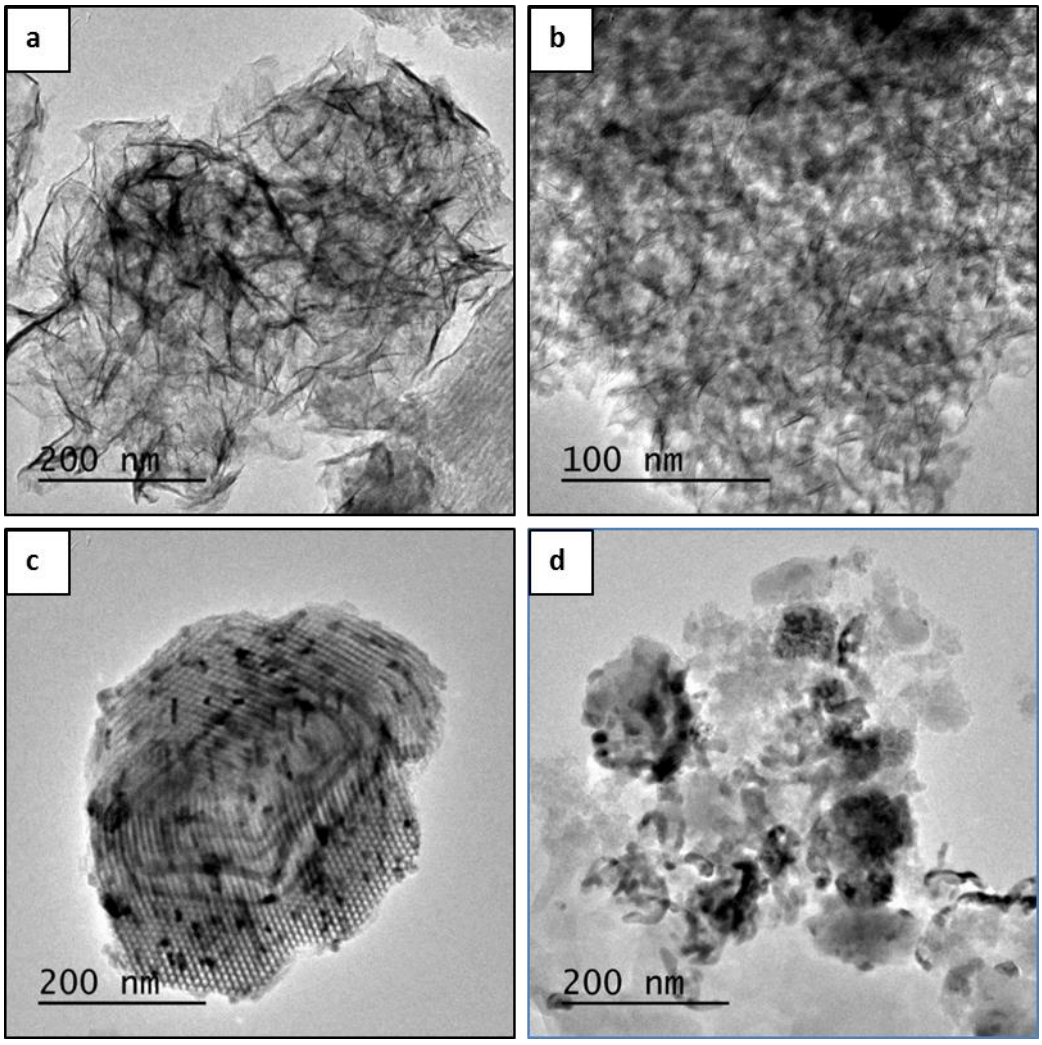


Figure 1. TEM images for calcined Ni/SBA-15 DP (a), Ni/$SiO_2$ DP (b), Ni/SBA-15 ImU(c), and Ni/$SiO_2$ ImU (d).

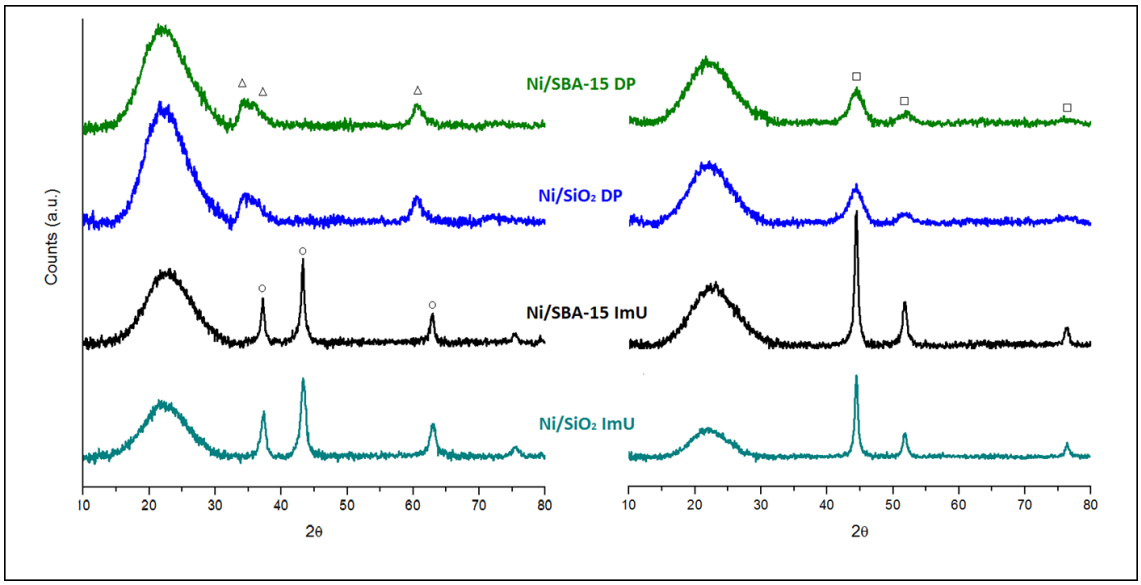


Figure 2. XRD patterns for (left) calcined and (right) treated in 5%$H_2$/Ar at 750 $^{o}$C nickel-based systems.

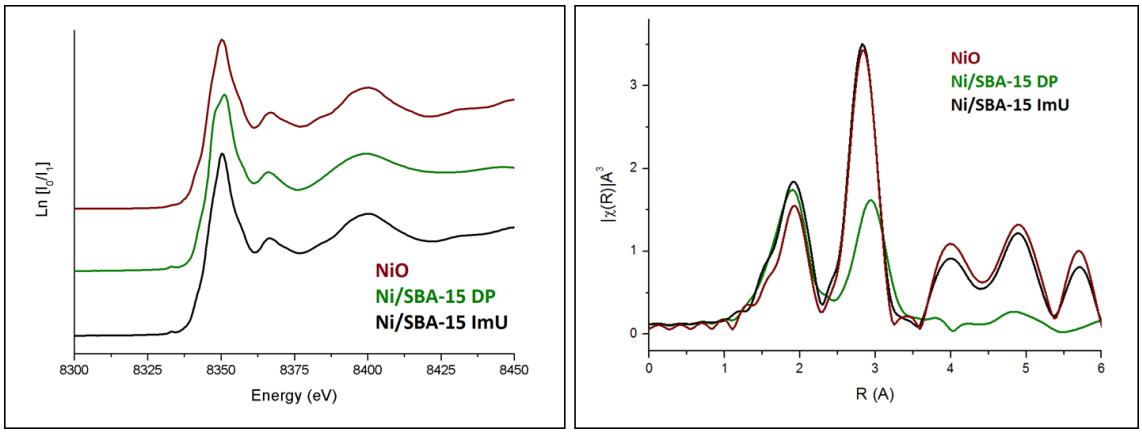


Figure 3. Ni-K edge XANES spectra (left) and Fourier Transform functions of the EXAFS oscillations (right) for calcined nickel-based systems supported in SBA-15.

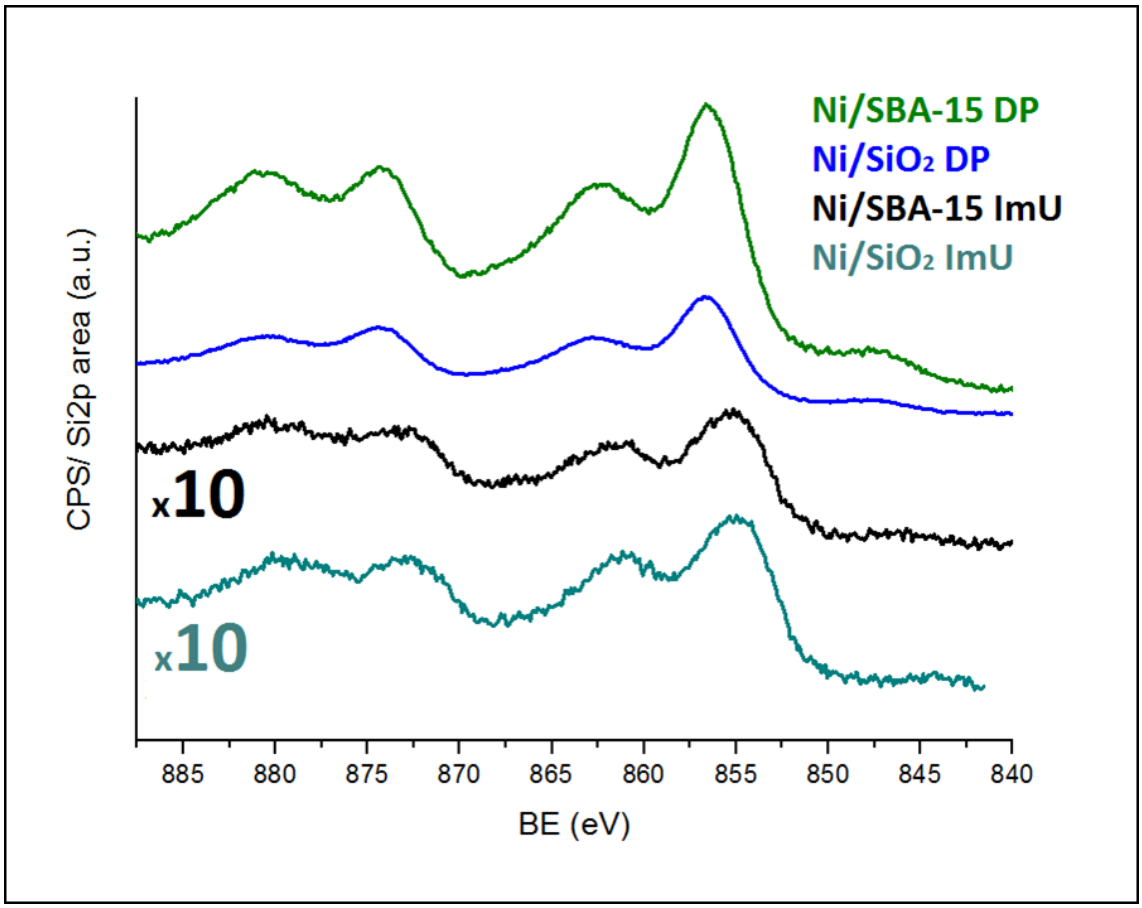


Figure 4. XPS spectra for calcined nickel-based systems.

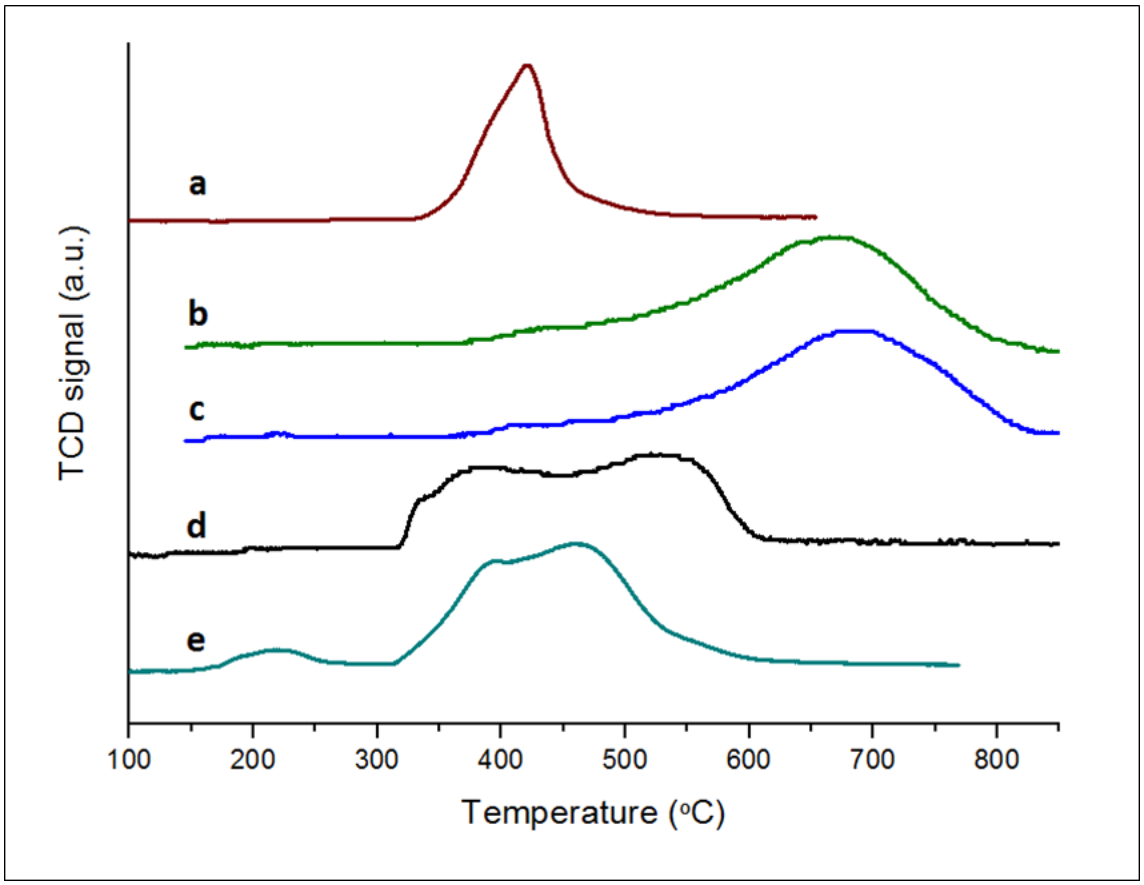


Figure 5. Temperature-programmed reduction profile for a NiO pattern (a), calcined Ni/SBA-15 DP (b), Ni/$SiO_2$ DP (c), Ni/SBA-15 ImU (d) and Ni/$SiO_2$ ImU (e).

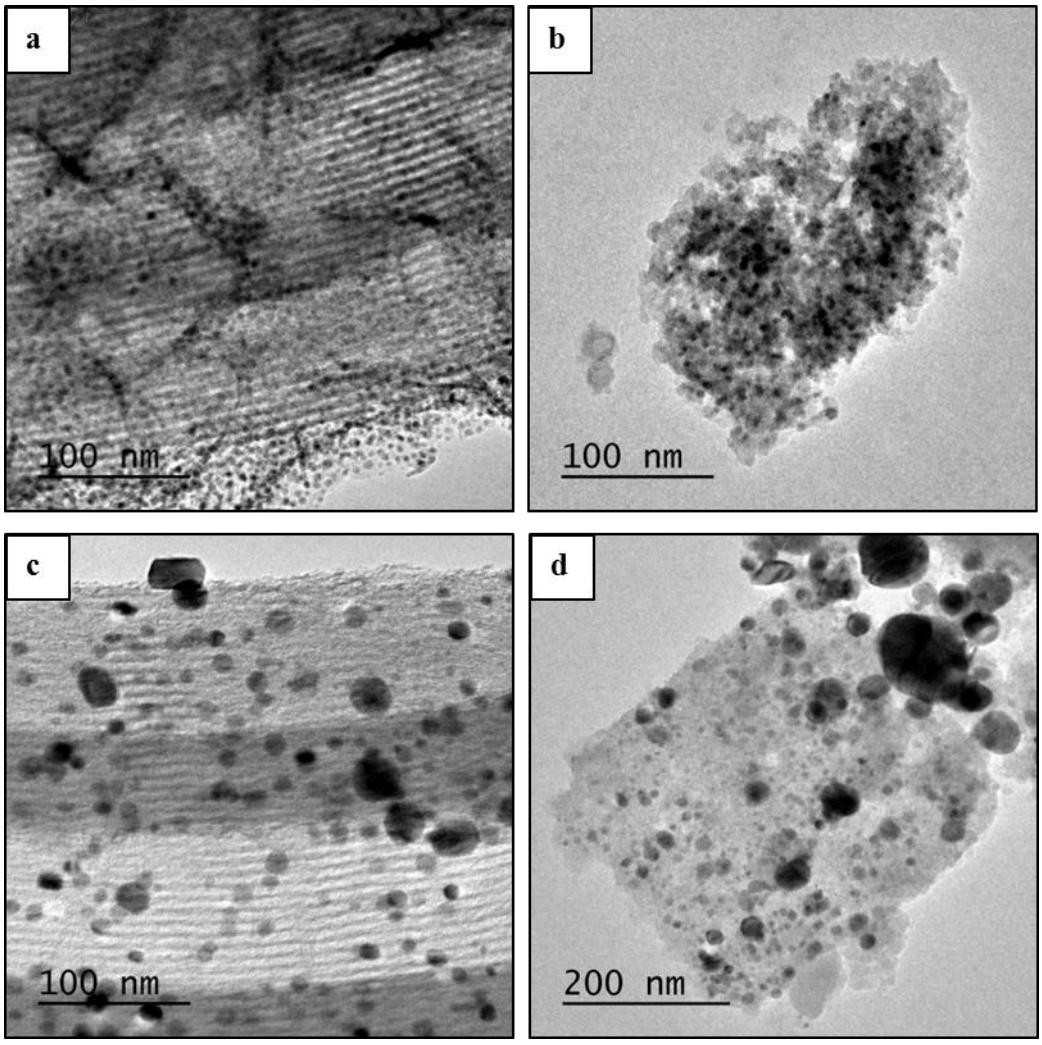


Figure 6. TEM images for reduced Ni/SBA-15 DP (a), Ni/$SiO_2$ DP (b), Ni/SBA-15 ImU(c), and Ni/$SiO_2$ ImU (d).

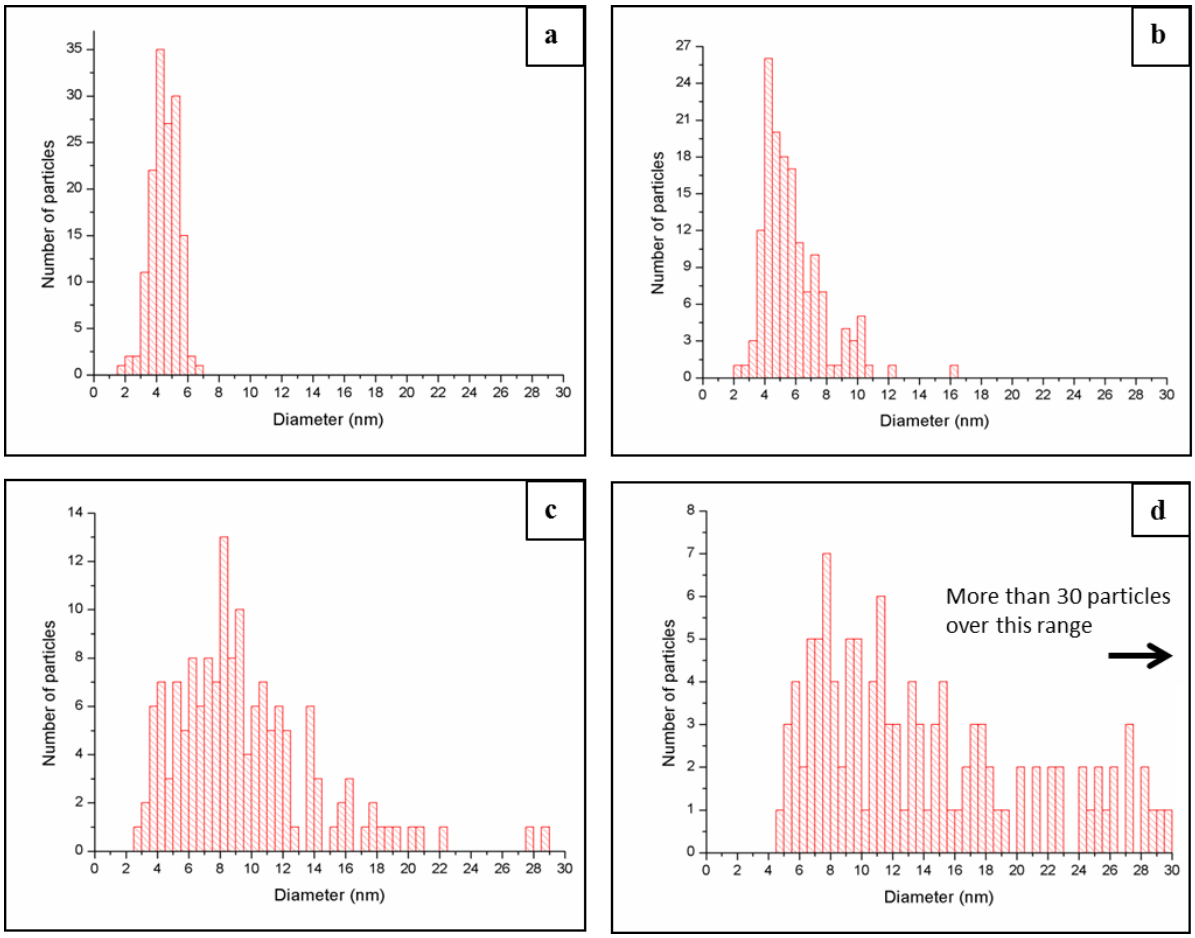


Figure 7. Particle size distribution for reduced Ni/SBA-15 DP (a), $Ni/SiO_2$ DP (b), Ni/SBA-15 ImU(c), and $Ni/SiO_2$ ImU (d).

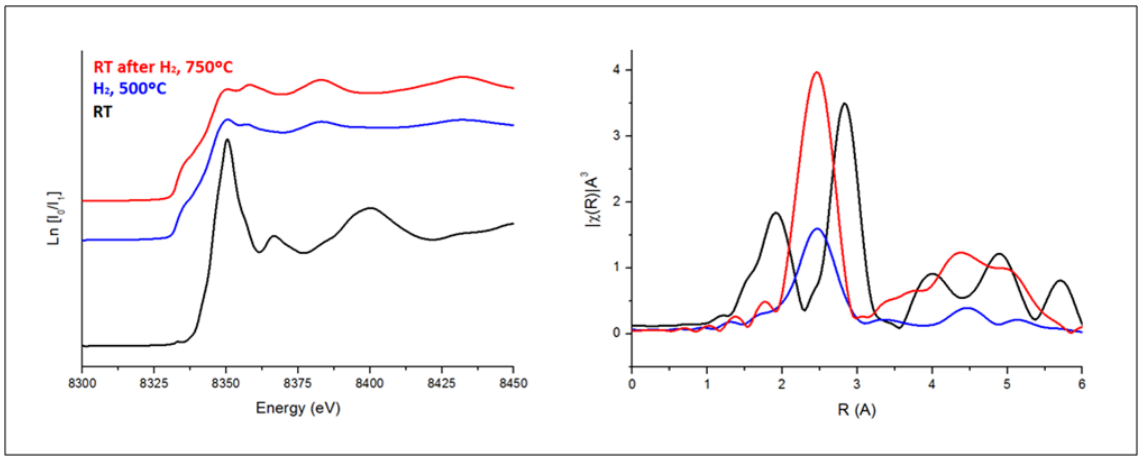


Figure 8. Ni-K edge XANES spectra (left) and Fourier Transform functions of the EXAFS oscillations (right) obtained for Ni/SBA-15 ImU during the indicated treatments.

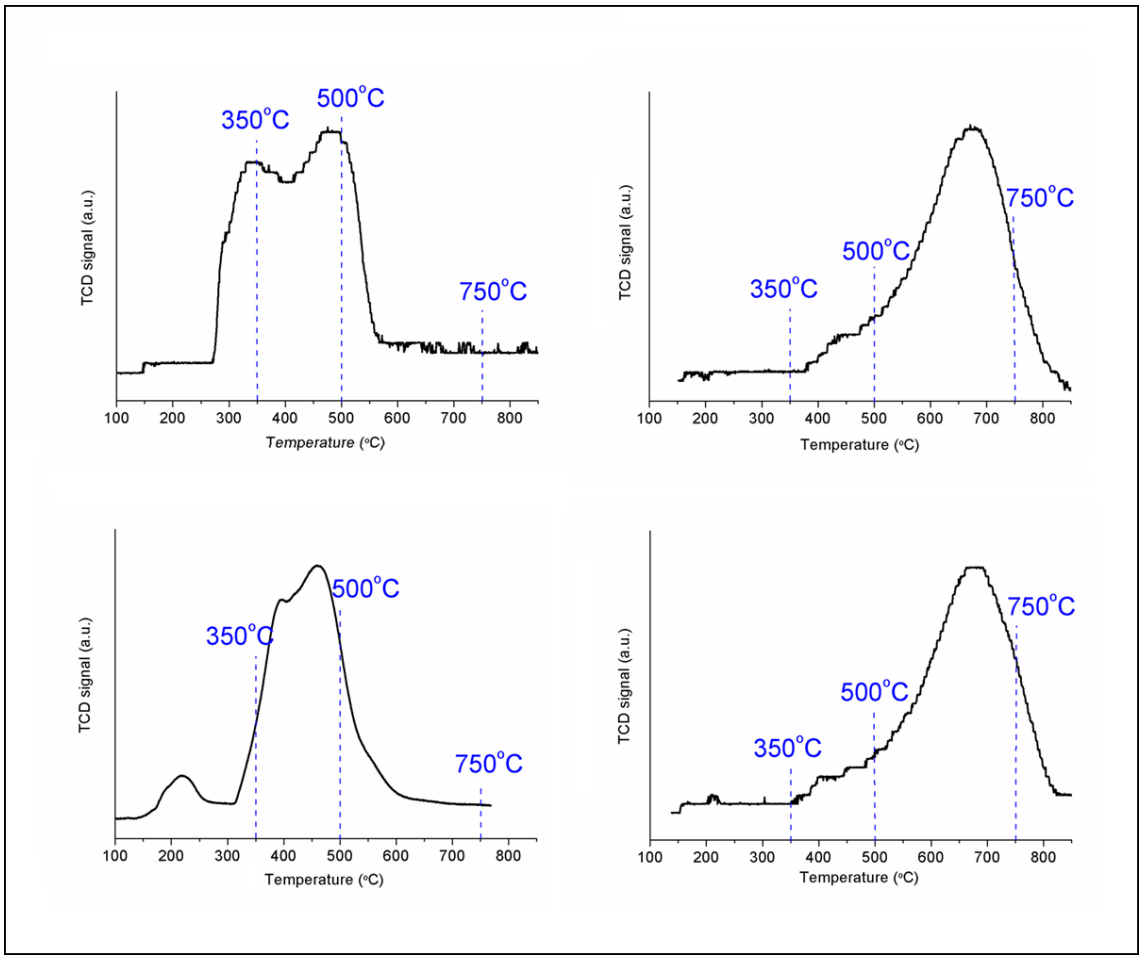


Figure 9. TPR profiles of the nickel supported systems

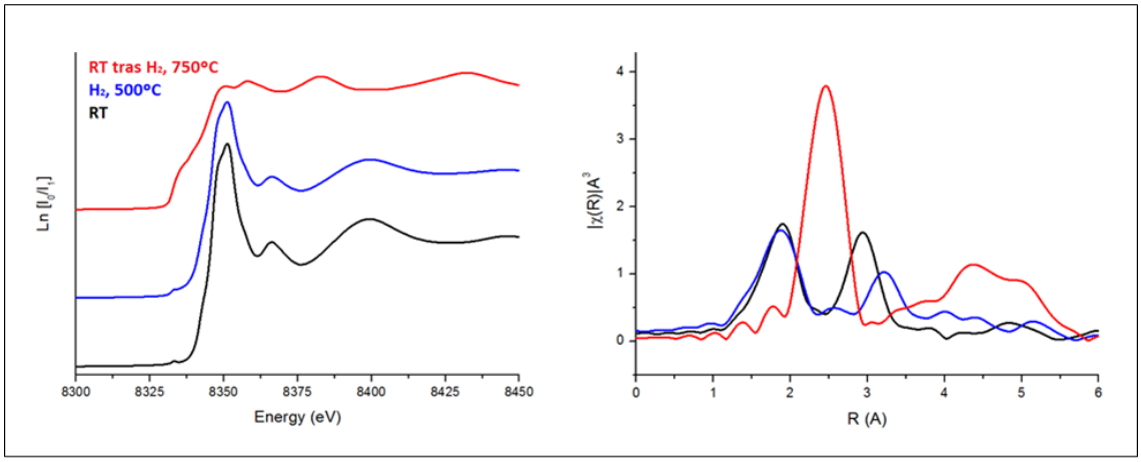


Figure 10. Ni-K edge XANES spectra (a) and Fourier transform functions of the EXAFS oscillations (b) obtained for Ni/SBA-15 DP during the indicated treatments.

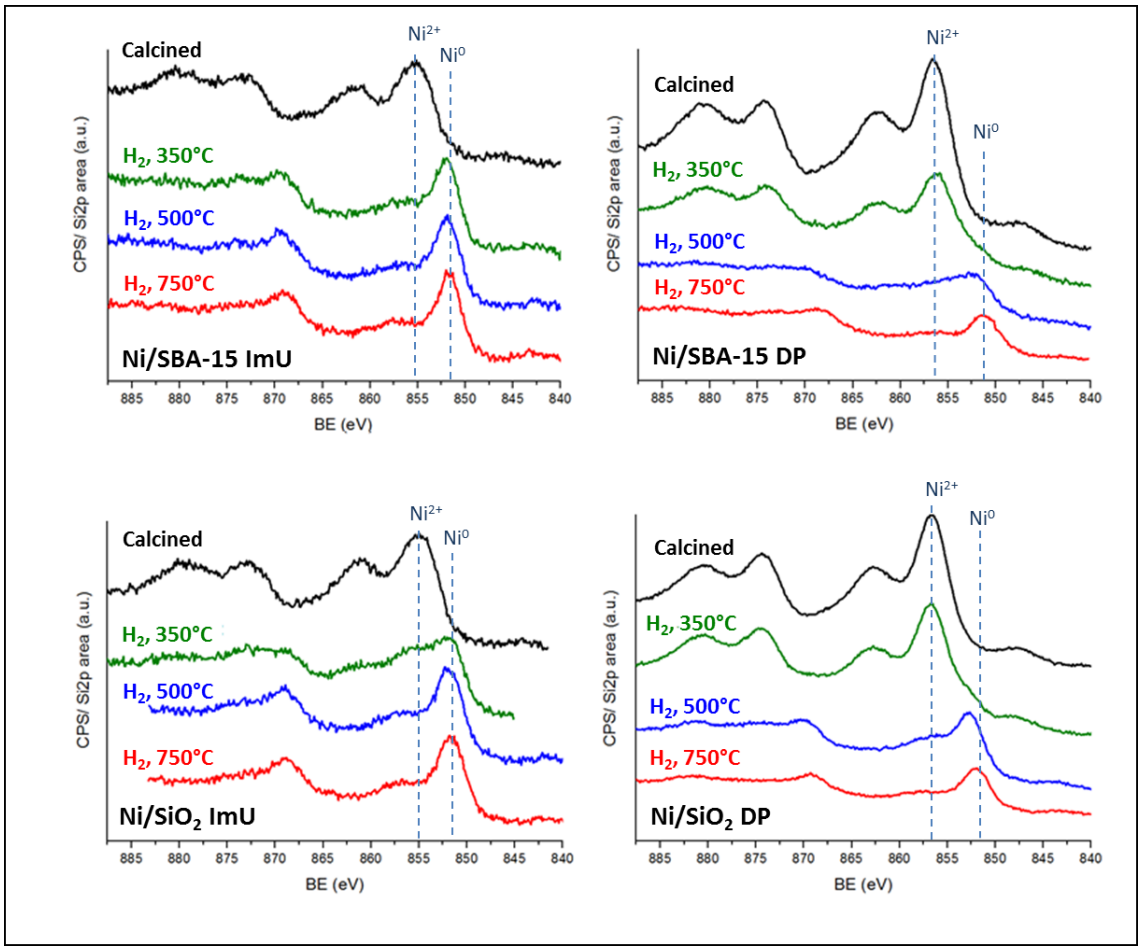


Figure 11. XPS spectra of nickel-based systems submitted to the indicated *in situ* treatments.

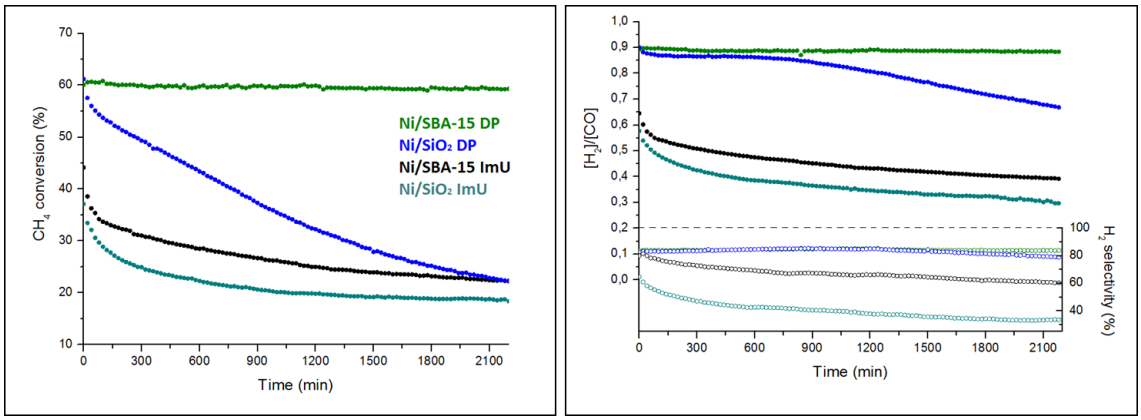


Figure 12. (left) $CH_4$ conversion in the reaction of DRM at 750 $^{o}$C using a mix of $CH_4$:$CO_2$ [1:1] with 80 mL/min as a total flow. (right) [$H_2$]/[CO] ratio and $H_2$ selectivity.

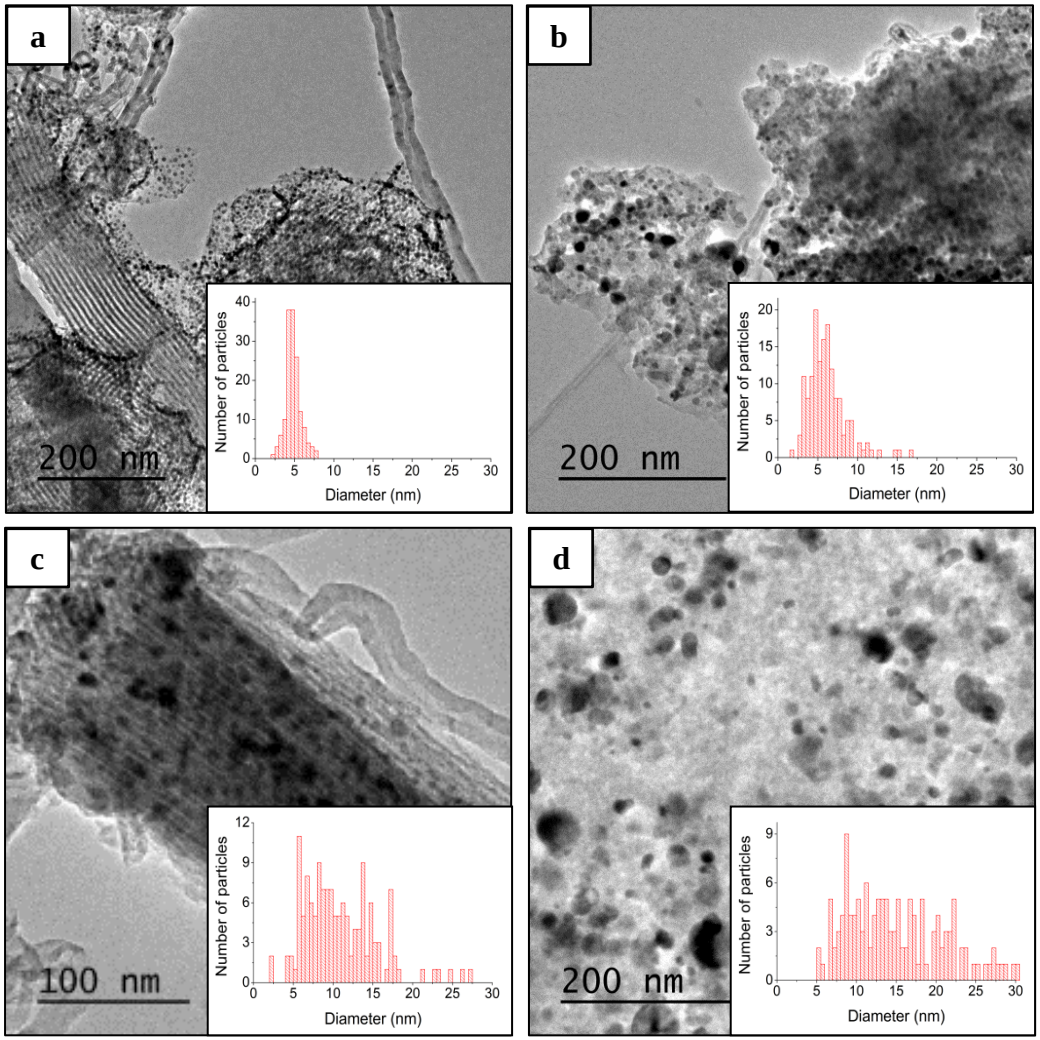


Figure 13. TEM images of Ni/SBA-15 DP (a), Ni/$SiO_2$ DP (b), Ni/SBA-15 ImU (c) and Ni/$SiO_2$ ImU (d) after DRM test.

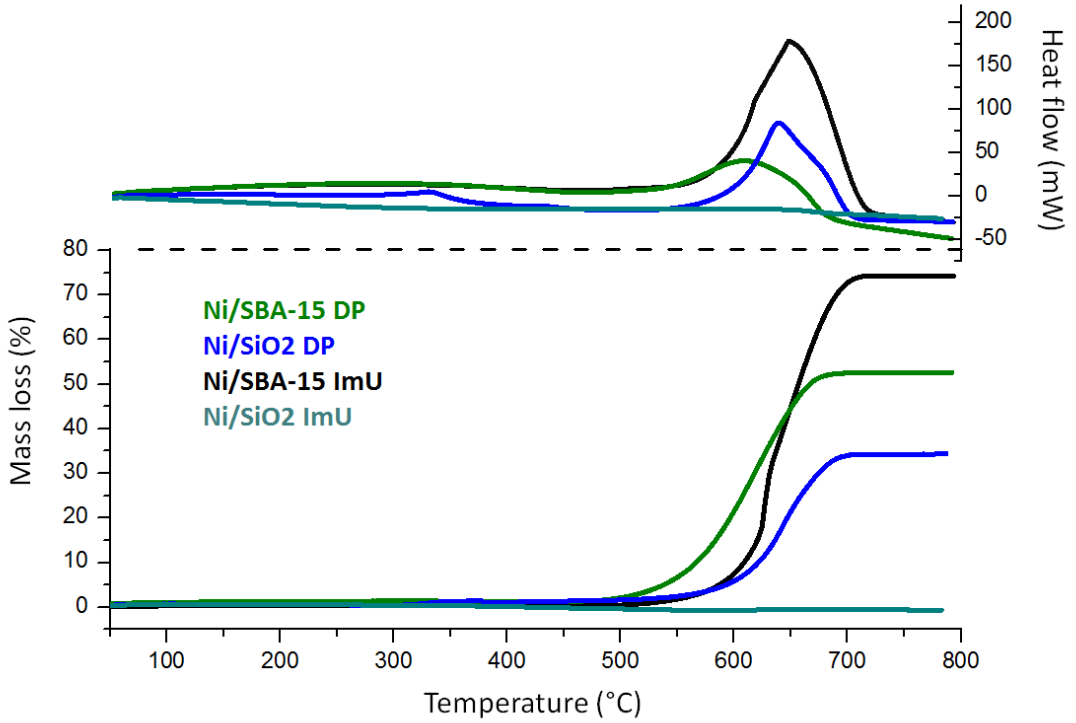


Figure 14. TG and DSC analysis performed in air flow for the catalytic systems after 40h in DRM.